

RSC Advances



This is an *Accepted Manuscript*, which has been through the Royal Society of Chemistry peer review process and has been accepted for publication.

Accepted Manuscripts are published online shortly after acceptance, before technical editing, formatting and proof reading. Using this free service, authors can make their results available to the community, in citable form, before we publish the edited article. This *Accepted Manuscript* will be replaced by the edited, formatted and paginated article as soon as this is available.

You can find more information about *Accepted Manuscripts* in the [Information for Authors](#).

Please note that technical editing may introduce minor changes to the text and/or graphics, which may alter content. The journal's standard [Terms & Conditions](#) and the [Ethical guidelines](#) still apply. In no event shall the Royal Society of Chemistry be held responsible for any errors or omissions in this *Accepted Manuscript* or any consequences arising from the use of any information it contains.

In₂O₃ cube: Synthesis, characterization and photocatalytic properties

Sheng-qi Guo,[†] Xiao Zhang,[†] Zhen-wei Hao,[†] Guan-dao Gao,^{*,†} Guang Li,^{*,‡} Lu Liu^{*,†}

[†] *Tianjin Key Laboratory of Environmental Remediation and Pollution Control, Nankai University, Tianjin 300071, China.*

[‡] *School of Physics and Materials Science, Anhui University, Hefei, Anhui 230039, China.*

KEYWORDS: In₂O₃, cube structure, microporous, photoluminescent, photocatalytic activity

Author information

* Corresponding author.

E-mail: gaoguandao@nankai.edu.cn; liguang1971@ahu.edu.cn; liul@nankai.edu.cn.

ABSTRACT: 3D cube microporous In_2O_3 have been successfully obtained by calcining the as-synthesized cube $\text{In}(\text{OH})_3\text{-InOOH}$ precursor at 300 °C for 2 hours. X-ray diffraction (XRD), scanning electron microscopy (SEM), and transmission electron microscopy (TEM) were employed to clarify their structures and morphologies of the both cube $\text{In}(\text{OH})_3\text{-InOOH}$ precursor and cube In_2O_3 . The formation mechanisms of $\text{In}(\text{OH})_3\text{-InOOH}$ precursor and cube In_2O_3 were investigated. As an important semiconductor photocatalytic material, its photocatalytic properties have been tested. Under the irradiation of UV light, the cube microporous In_2O_3 exhibits excellent photocatalytic property to degrade eosin B (EB), which presents ~95% degradation of EB after 3 hours and the degradation rates is as 10.5 times as that of commercial In_2O_3 powder. The high separation efficiency of electron-hole pairs results in the high photocatalytic activity. Furthermore, photoluminescent properties of the cube microporous In_2O_3 have been investigated as well.

1. INTRODUCTION

A large number of manufactured dyes were released into the water environment with the development of the industry.^{1,2} Most of dyes are resistant to biodegradation, and N-containing dyes undergo the anaerobic degradation to yield potentially carcinogenic aromatic amines.³ Therefore, a hot research activity has been devoted recently to search for semiconductor photocatalysts that directly degrade dyes in wastewater.^{4,5} The involved photocatalysts, are mostly based on metal oxide semiconductors, such as Bi_2O_3 , Nb_2O_5 , Ag_3PO_4 *etc.*⁶⁻⁹ As one of the most important semiconductor materials, indium oxide (In_2O_3) has been considered as a promising alternative in photocatalysis with the narrower band gap (~2.8 eV) as well as which can absorb wider solar spectral range than the popular TiO_2 (~3.2 eV).¹⁰⁻¹² Furthermore, owing to its nontoxicity and excellent stability, In_2O_3 has attracted obvious attention as a alternative photocatalytic material.¹³

As n-type semiconducting oxide of the III–VI compounds, In_2O_3 exhibits novel electronic and optical properties.¹⁴ Due to the low resistivity, high conductivity, high infrared light reflectivity and abundant defects on the surface,¹⁵⁻¹⁷ In_2O_3 has potential applications in computer touch screens,¹⁸ optoelectronic field,¹⁹ sensors^{13,20} and photocatalysis.²¹ Especially, In_2O_3 shows superior effect in photocatalysis degradation dyes. Many chemists have made great contributions to this

field. Shao et al. reported nanocube In_2O_3 /carbon nanofibers heterostructures with high visible light photocatalytic activity for degrading RhB.²² Cao and co-workers synthesized hollow In_2O_3 nanocrystals, which also exhibit excellent photocatalytic activities for degrading RhB and MB under UV irradiation.²³ Obviously, properties of materials can often be improved through the structure design. To meet different requirements, many nano- and micro-sized In_2O_3 with different morphologies including nanocolumns,²⁴ nanofibers,²⁵ nanorods,²⁶ nanosheets,²⁷ nanowires²⁸ and nanotubes²⁹ had been synthesized in succession in the past decade. These structures not only create intriguing variety of morphology features, but also provide good blocks for developing high photocatalytic performance.

In this article, we report a facile method for the preparation of cube $\text{In}(\text{OH})_3$ - InOOH precursor under mild conditions without any additives. After the precursor is calcined for 2 hours in air, microporous In_2O_3 cube structures are successfully obtained. The possible formation mechanism of cube $\text{In}(\text{OH})_3$ - InOOH precursor and cube microporous In_2O_3 are rationally proposed. Afterwards, photocatalytic performances of the as-prepared In_2O_3 are investigated and the cube microporous In_2O_3 exhibits significantly enhanced photocatalytic activity for degradation of eosin B (EB) molecules under UV light irradiation.

2. EXPERIMENTAL SECTION

Preparation of cube $\text{In}(\text{OH})_3$ - InOOH precursor and microporous In_2O_3 cube. All reagents are of analytic grade and were used without further purification. In a typical synthesis, a mixture of InCl_3 (0.2g) and Sodium oxalate (0.2g) in water was stirred for 30 min, and then sealed in a 30ml Teflon-lined stainless steel autoclave and heated at 150 °C for 1 h. After the sample was gradually cooled to room temperature, a white precipitate was collected and then washed with distilled water and absolute ethanol, and the sample was kept in absolute ethanol. The In_2O_3 structure was obtained by annealing the corresponding $\text{In}(\text{OH})_3$ - InOOH precursor in air at 300 °C for 2h.

Material Characterization. X-ray diffraction analysis of the samples were carried out by an X-ray diffractometer (XRD, Rigaka D/max2500) with Cu $K\alpha$ radiation ($\lambda = 1.54056 \text{ \AA}$). The morphology of the as-prepared products was characterized by scanning electron microscopy (SEM, Hitachi-530 or JEOLJSM-6700F) and transmission electron microscopy (TEM, JEOL-2010,

operating voltage of 200 kV). The Brunauer–Emmett–Teller (BET) specific surface area (SBET) of the sample was analyzed by nitrogen adsorption in a Tristar 3000 nitrogen adsorption apparatus, UV spectra were recorded on a Cary 5000 spectrometer at room temperature. Fluorescence spectrum was characterized by RPM2000.

Photocatalytic Reactions. The photocatalytic activities of the as-prepared microporous In_2O_3 cube structures were evaluated by the photocatalytic degradation of EB aqueous solution via an XPA-system Photochemical Reactor (Nanjing, China) at room temperature under ultraviolet light irradiation. A 300W Hg arc lamp was used as a light source to provide the UV light, the light intensity is $\sim 7 \text{ mw/cm}^2$. In a typical reaction, 0.05 g of as-prepared photocatalysts was dispersed into 50 mL of EB aqueous solution ($1 \times 10^{-5} \text{ M}$). Before light irradiating, the suspension was stirred for 1 hour in the dark to reach adsorption equilibrium of EB on the surface of cube structures. Then, the reaction was stopped at 1 hour intervals and 10 mL of reaction solutions were extracted to determine the concentrations of the aqueous EB solution by UV/vis spectroscopy. In this study, commercial In_2O_3 was used as a reference catalyst to photocatalytic EB under the same condition as the as-prepared samples. EB aqueous solution without photocatalysts irradiated by UV light was used as a blank experiment and the as-prepared photocatalysts reacting with EB in dark were used as comparative evaluation.

3. RESULTS AND ANALYSIS

3.1 Structural analysis of cube $\text{In}(\text{OH})_3$ - InOOH precursor and corresponding In_2O_3 structure

The phase structure of the obtained product was first investigated by X-ray diffraction (XRD). Figure 1 shows the XRD pattern of the as-prepared $\text{In}(\text{OH})_3$ - InOOH precursor. The XRD pattern indicates that the two types of crystals are the cubic $\text{In}(\text{OH})_3$ in space group Im-3 ($a=b=c= 7.974 \text{ \AA}$, JCPDS: 76-1463) and the orthorhombic InOOH in space group P21nm ($a= 5.260 \text{ \AA}$, $b= 4.560 \text{ \AA}$, $c= 3.270 \text{ \AA}$, JCPDS: 71-2283). The observed peaks of $\text{In}(\text{OH})_3$ could be assigned to diffraction from (200), (220), (222), (400), (420) and (422) faces. Meanwhile, the characteristic peaks of InOOH could be correspond to diffraction from the (110), (101), (011), (200), (021) and (121) faces. No impurities could be detected in the curve, suggesting high purity of the as-synthesized $\text{In}(\text{OH})_3$ - InOOH . The morphology of the resulting $\text{In}(\text{OH})_3$ - InOOH sample were investigated by

scanning electron microscopy (SEM) and transmission electron microscopy (TEM). As shown in figure 2a and 2b, the typical morphology of the as-prepared complex is cube structure with an average diameter of 600 nm. Figure 2c shows a typical TEM image of one surface of polyhedron crystal. As shown in the inset in Figure 2d, the crystalline lattice distances in the white frame are 2.82 Å and 3.44 Å, corresponding to the (220) face of cubic $\text{In}(\text{OH})_3$ and (110) face of orthorhombic InOOH , respectively, which are consistent with the XRD results.

/Insert Figure 1/

/Insert Figure 2/

Similar to other metal hydroxides,^{30,31} $\text{In}(\text{OH})_3$ – InOOH precursor cube can also be converted into In_2O_3 derivatives upon heating. From the TG-DSC result (Fig. S1), the calcination temperature was ascertained to be 300 °C. After calcining the as-synthesized cube $\text{In}(\text{OH})_3$ – InOOH precursor at 300 °C for 2 h in air, microporous In_2O_3 structure could be successfully obtained. Fig. 3 shows the corresponding XRD patterns of calcined products. All the diffraction peaks in this pattern could be indexed to a single phase of cubic In_2O_3 in space group $la\text{-}3$, which matches well with JCPDS: 06-0416 ($a=b=c=10.118$ Å). As shown in Figure 4a and 4b, the morphologies of the $\text{In}(\text{OH})_3$ – InOOH precursor were well transmitted to the product In_2O_3 besides pores structures, which indicates that the solid-state transformation of In_2O_3 from $\text{In}(\text{OH})_3$ – InOOH precursor by thermally decomposing is a topotactic process. In addition, the sample was characterized by TEM (Fig. 4c), and the low-magnification TEM images further clearly indicate that the sample has similar morphologies to the hydroxide precursors. However, many pores have been clearly observed inside the cube due to release of H_2O in the process of the decomposition of $\text{In}(\text{OH})_3$ – InOOH precursor. The HR-TEM images of an individual In_2O_3 cube was shown in Fig. 4d, which reveals that the crystalline lattice distances in the white frame are 4.13 Å, corresponding to the (211) crystalline plane of In_2O_3 .

/Insert Figure 3/

/Insert Figure 4/

BET gas sorptometry measurements were conducted to examine the porous nature of the In_2O_3 cube. As shown in Figure 5, the N_2 adsorption/desorption isotherm of the sample was identified as type II isotherm based on Brunauer-Deming-Deming-Teller (BDDT) classification, and the saturation adsorption platform at low P/P_0 indicated the presence of micropores in the sample. The

distribution of pore size indicates that a majority of the pores are smaller than 5 nm. These porous probably appeared among the surface of In_2O_3 cube and the gap by release of H_2O . The BET surface area reaches $71.41 \text{ m}^2\text{g}^{-1}$.

/Insert Figure 5/

3.2 Possible formation mechanisms of cube $\text{In}(\text{OH})_3$ - InOOH precursor and In_2O_3 structure

It is well known that the final morphology of crystal was controlled by the nature of crystal structure during the one stage of nucleation and the other stage of Ostwald ripening through the delicate affect of external factors, examples of the additive, concentration, reaction time and so on.³²⁻³⁴ Therefore, the final morphology of $\text{In}(\text{OH})_3$ - InOOH precursor are determined by the combination of internal and external factors.

Firstly, due to the process of synthesis without any organic additives or templates, the morphology of the final product is largely determined by the natural structure of $\text{In}(\text{OH})_3$ and InOOH . To the best of our knowledge, $\text{In}(\text{OH})_3$ crystallizes in cubic space group Im-3 and InOOH in orthorhombic space group P21nm . As demonstrated by Figure 6c and 6d, both $\text{In}(\text{OH})_3$ and InOOH crystallizes in distort cube structure. The fundamental building unit of $\text{In}(\text{OH})_3$ and InOOH consists of In_8O_{12} (Fig. 6a) and In_8O_8 (Fig. 6b) hexahedral structure, respectively, and each In_8O_{12} or In_8O_8 hexahedral structure sharing six planar quadrangle windows with six neighbors to generate the resulting 3D cube framework, which was also supported by the SEM and TEM observations. In addition, from the perspective of topology, each In atom connects six adjacent In atoms by O atoms and serves as a 6-connected node. Thus, the overall network of $\text{In}(\text{OH})_3$ - InOOH precursor can be described as a 6-connected **pcu** topology (Fig. 6e) with the Schläfli symbol of $4^{12}6^3$, which is a classic 3D cube structure topology.³⁵⁻³⁷ Consequently, the cube $\text{In}(\text{OH})_3$ - InOOH precursor along the a, b, c-axis in space are thermodynamically stable, and thus readily tends to form cube in shape due to their intrinsic hexahedral structure.

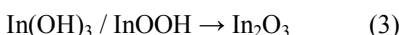
/Insert Figure 6/

Secondly, when we focused essentially on the influence by external factors, we found that the final morphology and size of $\text{In}(\text{OH})_3$ - InOOH precursor were strongly correlated to alkaline sources used. We conducted the alkaline-dependent experiments by changing different alkaline sources while the other experimental conditions unchanged. There is no regular product collected if sodium oxalate is replaced by ethylenediamine (Fig. 7a). Meanwhile, when NaOH or

hexamethylenetetramine were used as alkaline sources, irregular $\text{In}(\text{OH})_3\text{-InOOH}$ precursor were produced (Fig. 7b and 7c). Only when sodium oxalate was used as alkaline sources, the cube $\text{In}(\text{OH})_3\text{-InOOH}$ precursor with diameters of 600 nm was produced. To disclose the formation mechanism of $\text{In}(\text{OH})_3\text{-InOOH}$ precursor, further experiments exploring the effect of synthetic temperature on the formation of the morphology and size of $\text{In}(\text{OH})_3\text{-InOOH}$ precursor were investigated. The related results are shown in Fig. S2.

/Insert Figure 7/

On the basis of the above results, a growth process of the cube $\text{In}(\text{OH})_3\text{-InOOH}$ precursor and In_2O_3 may be illustrated as followed:



Firstly, the hydrolysis of the sodium oxalate results in the formation of OH^- ions, which provide a weak basic environment for the formation of Indium hydroxide crystal nucleuses. Subsequently, because of its nature cube structure, the crystal nucleuses of Indium hydroxide gradually grow into uniformly large cube due to the Ostwald ripening to reduce surface area and decrease the energy.

3.3 Optical Properties

The UV–vis diffuse reflectance spectra of cube In_2O_3 product is shown in Fig. 8, a strong absorption can be observed in the ultraviolet region. According to the plot of transformed Kubelka–Munk function versus the energy of exciting light, the value of the band gap for the cube In_2O_3 was estimated to be 2.7 eV.

/Insert Figure 8/

To investigate optical property of the sample, we measured the emission and excitation spectra shown in Fig.9a and 9b, in which Fig.9a is the emission spectrum of particles excited by 315 nm light. It can be found that the sample show wide-band emission in white range with a peak plat around 475 nm. It can be probably used as white lighting. As mentioned above, cube In_2O_3 is a semiconductor with an energy band $E_g = 2.7$ eV. When illuminated by 315 nm (about 3.95 eV in energy) light, electrons are excited into conduction band and then jump into valance band with strong emission at 444 nm (corresponding to 2.7 eV in energy) if just only taking band edge transition into consideration. The peak flat of emission at 475 nm is a slight red-shift phenomenon

that is widely observed for nano-particles. However, due to that the excited energy is much larger than 2.7 eV, the electrons are excited to higher levels than bottom of conduction band (-0.63 eV versus NHE), the emission spectrum are much complex including inter-band jumping from higher level (electrons) to higher levels (holes) , intra-band jumping from higher level (electrons) to bottom of conducting band, etc. This is the reason for the white emission. Fig.9b is the excitation spectrum of prepared In_2O_3 particles. There are many two peaks locating at 315nm and 365nm. The two absorption peaks may arise from the quantum transitions happening between the energy level of In^{3+} ions.

/Insert Figure 9/

3.3 Application in Photogradation of eosin B (EB)

Eosin B has been successfully used in surface-second harmonic generation studies of acid-base equilibrium,³⁸ and orientational relaxation at air/water interfaces, which belongs to xanthene family dye.³⁹ We assessed the potential validity of cube In_2O_3 for photocatalytic removal of EB. As a comparison, the EB photodegraded by commercial In_2O_3 was also performed. The characteristic absorption peak of EB at $\lambda = 514$ nm was selected as monitoring wave length. Control experiments revealed that the photodegradation of EB irradiated under UV light could almost be neglected in the absence of cube In_2O_3 . Also, there was no appreciable degradation of EB over the cube In_2O_3 after 5h in the absence of UV light irradiation. As observed in Figure 10a, with the increase of illumination time, the main absorption peak of EB gradually weakened. No other absorption bands appear in either the ultraviolet or visible region. After 3h irradiation under UV light, the photodegradation ratio of EB was about 95% (Fig. 10b). However, the photodegradation ratio of EB was only 33% in the presence of commercial In_2O_3 after 5h. Obviously, the as-prepared In_2O_3 exhibits better photocatalytic activity than commercial In_2O_3 . This is mostly ascribe to the larger BET surface area (cube In_2O_3 : 71.41 m^2/g ; commercial In_2O_3 : 20.33 m^2/g), which leads to more surface reaction sites.^{23,40} In particular, the microporous structure of the catalyst facilitates light waves to penetrate deep inside the photocatalyst and beget high mobility of charge, which also leads to higher catalytic activity.⁴¹⁻⁴³ Due to the low initial concentrations of the reactants (the initial concentration (c_0) = 10 mg/L for EB in the present experiment), the photocatalytic degradation of EB over the cube In_2O_3 follows pseudo-first-order based on the kinetic linear simulation,⁴⁴ that can be fitted to the equation:

$$\ln c_0/c = kt \quad (1)$$

where c_0 is the initial EB concentration, c indicates the EB concentration after irradiation time t , k is the reaction rate constant. In this system, the k for cube In_2O_3 and commercial In_2O_3 are $k_{\text{cube In}_2\text{O}_3}$ (1.0447h^{-1}) and $k_{\text{commercial In}_2\text{O}_3}$ (0.0991h^{-1}), respectively, which are also summarized in Fig.10c.

/Insert Figure 10/

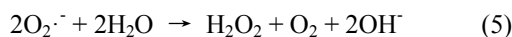
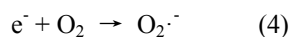
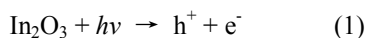
Moreover, the stability of photocatalysts is also one of most important factor from the practical viewpoint as well as its photocatalytic activity. Thus, recycle experiments were further investigated. After three recycles for the photodegradation of EB, the hierarchical microsphere photocatalysts did not exhibit significant loss of activity (Fig. 10d), indicating that these photocatalysts have relatively high stability during the photocatalytic oxidation of the dye.

3.4 Proposed degradation mechanism of EB

In order to monitor the active radicals that form during the photodegraded process, we first investigated the effect of band structure on the activity of the as-prepared In_2O_3 . We can calculate its conduction and valence band positions through the following equation: $E_{\text{CB}} = X - E_{\text{C}} - 1/2E_{\text{g}}$,⁴⁵ where X is the absolute electronegativity of the semiconductor. E_{C} is the energy of free electrons on the hydrogen scale (~ 4.5 eV). E_{g} is the band gap energy of the semiconductor. As a result, CB of In_2O_3 is -0.63 eV, which is 0.3 eV lower than that of $\text{O}_2 / \text{O}_2^{\cdot-}$ (-0.33 eV), which may facilitate for the $\text{O}_2^{\cdot-}$ generated to involve in degradation. The VB is estimated to be 2.07 eV, which is 0.08 eV higher than that of $\cdot\text{OH} / \text{OH}^-$ ($+1.99$ eV), suggesting that the hole photogenerated on the surface of In_2O_3 could react with $\text{OH}^- / \text{H}_2\text{O}$ to form $\cdot\text{OH}$ from the theoretical viewpoint.⁴⁶ To further confirm the presence of active radicals, the EB/ In_2O_3 system was examined by DMPO spin-trapped ESR spectroscopy. As shown in Fig. 11, there were no DMPO- $\cdot\text{OH}$ or DMPO- $\text{O}_2^{\cdot-}$ signal can be detected before irradiation. While after irradiation (15 min), characteristic four peaks of the DMPO- $\cdot\text{OH}$ adduct with intensity 1:2:2:1 were observed. However, when the irradiation time prolong to 30 min, the ESR signals disappeared. As for $\text{O}_2^{\cdot-}$, due to its unstable in aqueous solution and is easily decomposed into $\cdot\text{OH}$, we used methanol as solvent instead of water. It is shown in Fig 11b that $\text{O}_2^{\cdot-}$ signals were observed in the UV illuminated methanol solution of $\text{In}_2\text{O}_3/\text{EB}/\text{DMPO}$, confirming that $\text{O}_2^{\cdot-}$ also generated during the In_2O_3 photodegradation of EB.

/Insert Figure 11/

From our experimental results, a proposed degradation mechanism was being discussed to explain the enhancement of the photocatalytic properties of the cube In_2O_3 . According to the classic photocatalytic theory, cube In_2O_3 generate valence-band holes (h^+) and conduction-band electrons (e^-) pairs at the surface after absorbing an ultraviolet light energy $h\nu$, which is match the band gap energy (E_g) (reaction 1).⁴⁷ The h^+ could react with hydroperoxy adsorbed on the surface of cube In_2O_3 to generate highly reactive hydroxyl radicals ($\cdot\text{OH}$), which could direct reaction of the organic pollutants with surface light energy (reaction 2, 3).⁴⁸ On the other hand, the surface of cube In_2O_3 e^- could react with dissolved oxygen molecules to yield superoxide radical $\text{O}_2^{\cdot-}$. The superoxide radical $\text{O}_2^{\cdot-}$ react with water to produce hydroperoxy. Hydroperoxy is a key intermediate product for the latter route, which can easily break down and also provide conditions for subsequent produce $\cdot\text{OH}$ radicals (reaction 4-6). Therefore, large number of $\cdot\text{OH}$ radicals is resulting in the enhanced photocatalytic activity.⁴⁹⁻⁵¹



To further validate that the electron-hole pairs were easily separated and transferred to the surface of cube In_2O_3 under UV irradiation, the electrochemical impedance spectroscopy (EIS) were determined. The EIS spectra were completed using a potential amplitude of 5 mV over a frequency range of 0.1– 10^6 Hz and were simulated using the *Zview* software. The results (Fig. 12) reveal that the cube In_2O_3 has higher conductivity than commercial In_2O_3 , that is, in the case of cube In_2O_3 , the photoinduced electron-hole pairs were easily separated and transferred to the sample surface compared with commercial In_2O_3 .^{53,54} To obtain more detailed information, equivalent circuit can be designed for two kinds of In_2O_3 . From Table S1, it can be observed that the R_s of cube In_2O_3 is smaller than the R_s of commercial In_2O_3 , which leads to improved catalytic property of cube In_2O_3 .⁵⁵

/Insert Figure 12/

4. CONCLUSIONS

In summary, we prepared microporous In_2O_3 cube *via* two-step hydrothermal routes and a subsequent sintering process. The formation mechanism of $\text{In}(\text{OH})_3$ - InOOH cube precursor and In_2O_3 cube have been discussed in detail. The In_2O_3 cube exhibits excellent photocatalytic activities as photocatalyst for degeneration of EB under UV irradiation and its degradation rate is 10.5 times of that of commercial In_2O_3 powder due to its higher BET surface area. Researches on the photocatalytic mechanism indicate that the $\cdot\text{OH}$, $\text{O}_2\cdot^-$ and holes from the photocatalytic process are responsible together for its high photocatalytic performance. It is expected that this microporous materials will greatly promote their practical application to eliminate the dyes from wastewater.

Acknowledgements

This work was supported by the National Science Foundation of China (No. 21271108), the Ministry of Science and Technology (Grant 2014CB932001), 2011 Science Foundation of Tianjin (No. 11JCZDJC24800), and China–U.S. Center for Environmental Remediation and Sustainable Development.

REFERENCES

1. A. B. Dos Santos, F. J. Cervantes and J. B. van Lier, *Bioresour. Technol.*, 2007, 98, 2369–2385.
2. H. Zollinger, VCH Publishers: New York, 1987.
3. S. Horikoshi, F. Hojo and H. Hidaka, *Environ. Sci. Technol.*, 2004, 38, 2198–2208.
4. R. Asahi, T. Morikawa, T. Ohwaki, K. Aoki and Y. Taga, *Science*, 2001, 293, 269–271.
5. Z. Zou, J. Ye, K. Sayama and H. Arakawa, *Nature*, 2001, 414, 625–627.
6. M. Ge, Y. F. Li, L. Liu, Z. Zhou and W. Chen, *J. Phys. Chem. C*, 2011, 115, 5220–5225.
7. N. Kim, R. N. Vannier and C. P. Grey, *Chem. Mater.*, 2005, 17, 1952–1958.
8. S. X. Ge, H. M. Jia, H. X. Zhao, Z. Zheng and L. Z. Zhang, *J. Mater. Chem.*, 2010, 20, 3052–3058.
9. M. Ge, N. Zhu, Y. P. Zhao, J. Li and L. Liu, *Ind. Eng. Chem. Res.*, 2012, 51, 5167–5173.
10. J. B. Mu, B. Chen, M. Y. Zhang, Z. C. Guo, P. Zhang, Z. Y. Zhang, Y. Y. Sun, C. L. Shao and Y. C. Liu, *ACS Appl. Mater. Interfaces*, 2012, 4, 424–430.
11. Z. Y. Wang, B. B. Huang, Y. Dai, X. Y. Qin, X. Y. Zhang, P. Wang, H. X. Liu and J. X. Yu, *J. Phys. Chem. C*, 2009, 113, 4612–4617.
12. J. Lv, T. Kako, Z. S. Li, Z. G. Zou and J. H. Ye, *J. Phys. Chem. C*, 2010, 114, 6157–6162.
13. X. M. Xu, X. Li, W. B. Wang, B. Wang, P. Sun, Y. F. Sun and G. Y. Lu, *RSC Adv.*, 2014, 4, 4831–4835.
14. C. Q. Wang, D. R. Chen, X. L. Jiao and C. L. Chen, *J. Phys. Chem. C*, 2007, 111, 13398–13403.
15. Y. Zhang, H. Jia, D. Yu, X. Luo, Z. Zhang and X. Chen, *J. Mater. Res.* 2003, 18, 2793–2798.
16. I. Hamberg and C. G. Granqvist, *J. Appl. Phys.*, 1986, 60, R123–R160.
17. A. Datta, S. K. Panda, D. Ganguli, P. Mishra and S. Chaudhuri, *Cryst. Growth Des.*, 2009, 9, 113–117.
18. S. Parthiban, K. Ramamurthi, E. Elangovan, R. Martins and E. Fortunato, *Appl. Phys. Lett.*, 2009, 94, 212101–212101-3.
19. H. Cao, X. Qiu, Y. Liang, Q. Zhu and M. Zhao, *Appl. Phys. Lett.*, 2003, 83, 761–763.
20. N. Du, H. Zhang, B. Chen, X. Ma, Z. Liu, J. Wu and D. Yang, *Adv. Mater.*, 2007, 19, 1641–1645.
21. B. Li, Y. Xie, M. Jing, G. Rong, Y. Tang and G. Zhang, *Langmuir*, 2006, 22, 9380–9385.

22. J. B. Mu, C. L. Shao, Z. C. Guo, M. Y. Zhang, Z. Y. Zhang, P. Zhang, B. Chen and Y. C. Liu, *J. Mater. Chem.*, 2012, 22, 1786–1793.
23. J. F. Yin and H. Q. Cao, *Inorg. Chem.*, 2012, 51, 6529–6536.
24. P. Guha, S. Kar and S. Chaudhuri, *Appl. Phys. Lett.*, 2004, 85, 3851–3853.
25. C. H. Liang, G. W. Meng, Y. Lei, F. Phillipp and L. D. Zhang, *Adv. Mater.*, 2001, 13, 1330–1333.
26. Z. X. Cheng, X. B. Dong, Q. Y. Pan, J. C. Zhang and X. W. Dong, *Mater. Lett.*, 2006, 60, 3137–3140.
27. X. M. Xu, D. W. Wang, W. B. Wang, P. Sun, J. Ma, X. H. Liang, Y. F. Sun, Y. G. Ma and G. Y. Lu, *Sens. Actuators, B*, 2012, 171–172, 1066–1072.
28. Y. F. Hao, G. W. Meng, C. H. Ye and L. D. Zhang, *Cryst. Growth Des.*, 2005, 5, 1617–1621.
29. C. L. Chen, D. R. Chen, X. L. Jiao and C. Q. Wang, *Chem. Commun.*, 2006, 4632–4634.
30. D. Li, X. C. Duan, Q. Qin, H. M. Fan and W. J. Zheng, *J. Mater. Chem. A*, 2013, 1, 12417–12421.
31. S. M. Yuan, J. X. Li, L. T. Yang, L. W. Su, L. Liu and Z. Zhou, *ACS Appl. Mater. Interfaces*, 2011, 3, 705–709.
32. J. M. Ma, J. Q. Yang, L. F. Jiao, Y. H. Mao, T. H. Wang, X. C. Duan, J. B. Lian and W. J. Zheng, *CrystEngComm*, 2012, 14, 453–459.
33. J. M. Ma, Y. P. Wang, Y. J. Wang, P. Peng, J. B. Lian, X. C. Duan, Z. F. Liu, X. D. Liu, Q. Chen, T. I. Kim, G. Yao and W. J. Zheng, *CrystEngComm*, 2011, 13, 2369–2374.
34. J. M. Ma, X. D. Liu, J. B. Lian, X. C. Duan and W. J. Zheng, *Cryst. Growth Des.*, 2010, 10, 2522–2527.
35. E. V. Alexandrov, V. A. Blatov, A. V. Kochetkov and D. M. Proserpio, *CrystEngComm*, 2011, 13, 3947–3958.
36. O. Delgado-Friedrichs, M. D. Foster, M. O’Keeffe, D. M. Proserpio, M. M. J. Treacy and O. M. Yaghi, *J. Solid State Chem.*, 2005, 178, 2533–2554.
37. I. A. Baburin, V. A. Blatov, L. Carlucci, G. Ciani and D. M. Proserpio, *Cryst. Growth Des.*, 2008, 8, 519–539.
38. A. A. Tamburello-Luca, P. Hebert, R. Antoine, P. F. Brevet and H. H. Girault, *Langmuir*, 1997, 13, 4428–4434.

39. P. Fita, M. Fedoseeva and E. Vauthey, *J. Phys. Chem. A*, 2011, 115, 2465–2470.
40. L. Zhou, W. Wang, H. Xu, S. Sun and M. Shang, *Chem.–Eur. J.*, 2009, 15, 1776–1782.
41. X. C. Wang, J. C. Yu, C. M. Ho, Y. D. Hou and X. Z. Fu, *Langmuir*, 2005, 21, 2552–2559.
42. C. S. Guo, M. Ge, L. Liu, G. D. Gao, Y. C. Feng and Y. Q. Wang, *Environ. Sci. Technol.*, 2010, 44, 419–425.
43. L. Z. Zhang, and J. C. Yu, *Chem. Commun.*, 2003, 16, 2078–2079.
44. M. Lee, S. Park, G. Lee, C. Ju and S. Hong, *Catal. Today*, 2005, 101, 283–290.
45. T. B. Li, G. Chen, C. Zhou, Z. Y. Shen, R. C. Jin and J. X. Sun, *Dalton Trans.*, 2011, 40, 6751–6758.
46. H. B. Fu, C. S. Pan, W. Q. Yao and Y. F. Zhu, *J. Phys. Chem. B*, 2005, 109, 22432–22439.
47. C. S. Pan and Y. F. Zhu, *Environ. Sci. Technol.*, 2010, 44, 5570–5574.
48. S. H. Yoon and J. H. Lee, *Environ. Sci. Technol.*, 2005, 39, 9695–9701.
49. M. M. Cheng, W. H. Ma, J. Li, Y. P. Huang, J. C. Zhao, Y. X. Wen and Y. M. Xu, *Environ. Sci. Technol.*, 2004, 38, 1569–1575.
50. S. Sato, *Langmuir*, 1988, 4, 1156–1159.
51. S. Q. Guo, X. Zhang, Z. Zhou, G. D. Gao and L. Liu, *J. Mater. Chem. A*, 2014, 2, 9236–9243.
52. L. Zhang, H. Fu and Y. Zhu, *Adv. Funct. Mater.*, 2008, 18, 2180–2189.
53. S. Zhu, T. Xu, H. Fu, J. Zhao and Y. Zhu, *Environ. Sci. Technol.*, 2007, 41, 6234–6239.
54. M. Y. Liu, G. Li and X. S. Chen, *ACS Appl. Mater. Interfaces*, 2014, 6, 2604–2610.

Figure Captions

Figure 1. XRD pattern of the synthetic $\text{In}(\text{OH})_3\text{--InOOH}$ precursor.

Figure 2. SEM images of the synthetic $\text{In}(\text{OH})_3\text{--InOOH}$ precursor: (a) high magnification, (b) low magnification. TEM images of the synthetic $\text{In}(\text{OH})_3\text{--InOOH}$ precursor: (c) low magnification, (d) high magnification and HRTEM image (insert) of the $\text{In}(\text{OH})_3\text{--InOOH}$ precursor.

Figure 3. XRD pattern of the synthetic cube In_2O_3 .

Figure 4. SEM images of the cube In_2O_3 : (a) high magnification, (b) low magnification. TEM images of the cube In_2O_3 : (c) low magnification, (d) HRTEM image.

Figure 5. N_2 adsorption/desorption isotherm and Barrett-Joyner-Halenda (BJH) pore size distribution plot (inset) of In_2O_3 .

Figure 6. (a) A schematic view of fundamental building unit of $\text{In}(\text{OH})_3$ with In_8O_{12} hexahedral structure and (b) In_8O_8 hexahedral structure of InOOH ; (c) Perspective view of 3D framework of $\text{In}(\text{OH})_3$ and (d) InOOH ; (e) Schematic representation of **pcu** topology with the Schläfli symbol of $4^{12}6^3$.

Figure 7. SEM images of the $\text{In}(\text{OH})_3\text{--InOOH}$ precursor prepared using different alkaline sources (a) ethylenediamine, (b) NaOH, (c) hexamethylenetetramine.

Figure 8. UV-vis diffuse reflectance of In_2O_3 ; the inset in the upper right is the absorption^{1/2} versus energy curve.

Figure 9. The emission (a) and excitation spectra (b) of cube In_2O_3 .

Figure 10. (a) Absorption spectra of a solution of EB in the presence of cube In_2O_3 and under exposure to UV light, (b) Time course of the decrease in the dye concentration using different catalysts, (c) Corresponding selected fitting results using pseudo-first-order reaction kinetics. (d) Cycling runs in the photocatalytic degradation of EB by cube In_2O_3 products.

Figure 11. (a) EPR spectra of DMPO- $\cdot\text{OH}$ adducts for $\text{In}_2\text{O}_3/\text{EB}$ dispersion in water, (b) DMPO- $\text{O}_2\cdot^-$ adducts for $\text{In}_2\text{O}_3/\text{EB}$ dispersion in methanol.

Figure 12. Nyquist plots of the dummy cell fabricated with cube In_2O_3 (a) and commercial In_2O_3 (b). The equivalent circuit used to fit the EIS of cube In_2O_3 (c) and commercial In_2O_3 (d).